Automotive Experiences
Vol. 7 No. 2 (2024) pp. 357-373
p-ISSN: 2615-6202 e-ISSN: 2615-6636

Research Paper

Numerical Study of Surface Flow for Ahmed Body in Crosswind Conditions

Pham Van Duy[1], Le Dinh Anh[2], Dinh Cong Truong[1], Tran The Hung[3], Do Van Minh[4]

[1]School of Mechanical Engineering, Hanoi University of Science and Technology, 1 Dai Co Viet Road, Hai Ba Trung, 11615, Vietnam
[2]VNU-University of Engineering and Technology, Vietnam National University, 144 Xuanthuy, Caugiay, 100000, Vietnam
[3]Faculty of Aerospace Engineering, Le Quy Don Technical University, 236 Hoang Quoc Viet, Bac Tu Liem, 100000, Vietnam
[4]Faculty of Special Equipments, Le Quy Don Technical University, 236 Hoang Quoc Viet, Bac Tu Liem, 100000, Vietnam

minhdv100@gmail.com

https://doi.org/10.31603/ae.11591

Published by Automotive Laboratory of Universitas Muhammadiyah Magelang

Article Info
Submitted: 19/06/2024
Revised: 13/08/2024
Accepted: 18/09/2024
Online first: 26/09/2024

Abstract

This study investigates standard vehicles' flow behavior and drag during crosswind conditions by a numerical approach. The model is a half-scaled Ahmed body with a slant angle of 25°. Reynolds Average Navier-Stokes equations with turbulent model k-ω SST is applied to solve Navier Stokes equation by discrete method. Experimental data validated the numerical results at the same flow conditions. The results indicated that the model's drag increases with yaw angles, which is connected with the development of the longitudinal vortex on the windward side. However, the lift coefficient and pressure drag acting on the slant showed a maximum value at a yaw angle of around 35° before they dropped again. The drop of those coefficients results in the moving upward of the longitudinal vortex above the slant. The complex vortex structures around the base in both cross-sectional and symmetric planes are analyzed. The skin-friction pattern and pressure distribution on the slant are exposed to understand the effect of the yaw angle on aerodynamic forces.

Keywords: Ahmed body; Yaw angle; Skin friction; Separation bubble; Longitudinal vortex

1. Introduction

Reducing air resistance and improving the aerodynamic performance of flying objects and vehicles are crucial tasks recently. So far, most energy sources are from fuel oil, which creates a large of dangerous emissions during the operation of the vehicles. This problem is significant in the urban area, where the population is high. Although electric vehicles are designed, the vehicles are in the developing process with limited use. Since the aerodynamic force is proposed to be the square of vehicles' velocity, reducing aerodynamic force is an essential approach for decreasing drag on highways in comparison to using a more powerful engine. By an estimation, reducing 50% drag results in saving 4% fuel consumption [1].

To investigate the aerodynamics of vehicles, many models have been built and used widely [2]–[4]. The Ahmed body, which was developed by Ahmed in 1984 [2], has become a standard model for studying aerodynamic characteristics. The model has a simple rectangular shape of the main body and a changeable slant angle at the rear part. Since the slant angle can be changed, flow is highly modified [5]. Additionally, the model is characterized by different types of vehicles. With a slant angle of 25°, the flow on the slant surface of Ahmed's body is characterized by a large separation flow around the middle plane, two

longitudinal vortexes, and a large wake flow. The large structure of the separation bubble and the longitudinal vortexes form a low-pressure region on the slant, which contributes to a high drag level. As the slant angle continues to increase, the separation bubble and longitudinal vortexes can break down, resulting in a sudden drag reduction [2], [6]. The generation and interaction between the separation bubble and the longitudinal vortexes have been focused on in various previous studies for understanding the drag behavior and proposing a control strategy [6]–[9].

The other issue for a vehicle is its moving in crosswind conditions. Generally, the crosswind occurs on every road and can become significant in critical conditions. Moving at a velocity of 100 km/s and crosswind of 8 angles, the cross velocity is around 20 km/h, which likely occurs practically [10]. The effect of crosswind on aerodynamic drag of vehicles has been studied widely by [6], [11], [12]. Millan et al. [11] measured the drag of Ahmed's body with yaw angles from 0 to 90° by a step of 5. They observed that the drag increases up to a yaw angle of 60°, then remained nearly constant before it increases at the yaw angle above 75°. However, the other aerodynamic parameters such as lift, side force, and flow behavior, were not investigated. By a small step of yaw angles and a global skin-friction measurement technique, Tran et al. [9] observed that the drag remains constant for yaw angles below 5°, and then it increases again. The constant value of drag is connected with a small change in the flow on the slant. At high yaw angles, the longitudinal vortex formed on the root upper surface is mixed with the longitudinal vortexes on the slant at the windward side to form a large separation flow with high aerodynamic drag. The flow above the slant and wake structure was studied by Tunay et al. [13] using both experimental and numerical methods, and Meile et al. [14] by particle image velocimetry measurements. However, since the experimental setup is complicated, measurements were conducted on some surfaces for limited parameters, such as force, pressure, or surface flow. Additionally, the oil flow visualization technique was mainly used by experimental methods for analyzing surface flow.

Recently, with the development of technology, computational fluid dynamics has become an important tool for solving fluid mechanics problems. Many mathematical models have been developed to solve the Navier-Stokes equation by discrete methods and provide different levels of accuracy. Although direct numerical simulation provides the highest accuracy level, the requirement for mesh size and step time prevents using it in real applications. Alternatively, Reynolds averaged Navier-Stokes equations provide acceptable results with saving numerical times although the turbulent model and parameters should be carefully adjusted. The RANS is, therefore, applied widely in many current studies [8], [15].

A summary of the previous studies for the 25° Ahmed body during yaw angle is summarized in **Table 1**. As reviews, although many studies were conducted for the Ahmed body, the experiments were conducted for limited cases with some limited parameters. Numerical study allows to extend results. However, the RANS method can not capture well the surface flow on the 25° Ahmed body [16], [17]. The modification of the RANS simulation with suitable numerical parameters should be developed. Additionally, simulation in a wide range of yaw angles should be conducted to fully understand the drag trend and related flow behavior, pressure distribution on the slant, and wake flow of the model.

In this study, we applied a simulation method for analyzing flow on the slant surface of the Ahmed body in a wide range of yaw angles. The main purpose of the study is to select parameters for the 25° Ahmed body and to analyze flow on a slant in a wide range of yaw angles. RANS turbulent model k - ω SST with modification of numerical parameters is applied for visualizing surface flow and exposing the aerodynamic characteristics of the model. The results indicated that by modification of parameters, the method can provide sufficiently accurate surface flow. The drag of the model increases with yaw angles. However, the lift increases to yaw angles around 35° and decreases at higher angles. The trend of pressure drag acting on the slant shows a similar pattern to the lift, which is shown first time in this study. The flow fields and pressure distribution on the slant are extracted for a detailed understanding of the drag trend and related flow behavior. This study provides systematic results and the relation between drag and flow behavior for a wide range of yaw angles, which were not

presented previously by experimental and numerical studies. We also present that the lift of the model and pressure drag acting on the slant decrease at a yaw angle above 35°, which is due to the movement of longitudinal vortexes and flow behavior at the upper surface. Additionally, with increasing yaw angles, it was found that the separation bubble decreases in size at disappears at the yaw angles of 40°.

2. Model Geometry and Numerical Method

2.1. *Model and meshing*

The model used in this study is a half-scaled Ahmed body, which is the same as the previous experimental study by Tran et al. [9]. The use of a model is helpful for the validation and comparison of the results. The based-height Reynolds number of the model in the current study is Re= 2×10^5. Although the size of the model is smaller than the standard Ahmed body, the characteristics of flow are similar for Reynolds numbers higher than 2×10^5. The dimension of the model is shown in **Figure 1**. In both experimental tests and numerical studies, the model is supported in the ground by four legs at the bottom position.

The numerical domain is shown in **Figure 1b**. The numerical domain has a size of 47.4 H × 18.0 H × 9.3 H in length, width, and height to capture detailed flow structure around the model at a range of yaw angles from 0 to 45°. A total of 11 yaw angles was used in this study to understand the drag trend and flow behavior around the slant surfaces and to obtain the aerodynamic drag trend of the model. The inlet is set up at velocity-inlet, and the outlet is set up at pressure outlet. Other regions are chosen as wall functions. Since the velocity is low, the air density and viscosity are considered constant values.

Unstructured poly mesh is used in this study. The mesh is generated by Meshing software by Ansys Company. Around the model, 15 uniform layers are used to capture the boundary layer. The thickness of the first layer is 0.1 mm. Far the model, the mesh volume increases to reduce the total mesh size. The mesh volume increases for the model to reduce the total mesh size. The structure of the mesh around the model is shown in **Figure 2**. The maximum value of y^+ is around 4.0 in this study (**Figure 2b**).

Table 1. Previous studies of the Ahmed body in cross-wind conditions

Investigators	Slant angle φ (°)	Yaw angle β (°)	Reynolds number, Re_H	Measurement technique	Main results of drag and flow
Tsai et al. [18]	Car model	0	2.7×10^4	Numerical simulation, RANS	Deflector reduces lift and noise
Meile et al. [14]	25, 35	-25–25	7.53×10^5	Force balance, pressure measurement	Drag remains constant at $\varphi = 25°$ and $\beta = -25–25°$
Tunay et al. [19]	25, 35	0–15	1.4×10^4	Flow visualization, PIV	Wake flow with a high turbulence rate is sensitive to crosswind.
Bello-Millan et al. [11]	25	0–90		Force measurement	Drag increases with β, but only force was measured
Rao et al. [20]	25, 35	0–15	5.5×10^5	Numerical simulation	A large low-pressure region is formed on the slant surface during crosswind conditions. Low pressure occurs on the windward side at $\beta = 10°$
Nakashima et al. [21]	32	0–15 step 1	8.3×10^4, 3.0×10^5	PIV, force balance	A sudden increase in drag occurs at β between 5° and 10°
Cheng et al. [22]	35	0–12 step 2	7.45×10^5	Force balance, pressure measurement	The deflector changes pressure near the shoulder.
Viswanathan [23]	35	0, 4, 8	7.45×10^5	Numerical simulation, RANS	Vortex generators reduce drag by around 8.5% at yaw conditions.
Tran et al. [9]	25	0, 3, 5, 8	2.0×10^5	Force balance, GLOF	Drag increases at $\beta > 5°$.

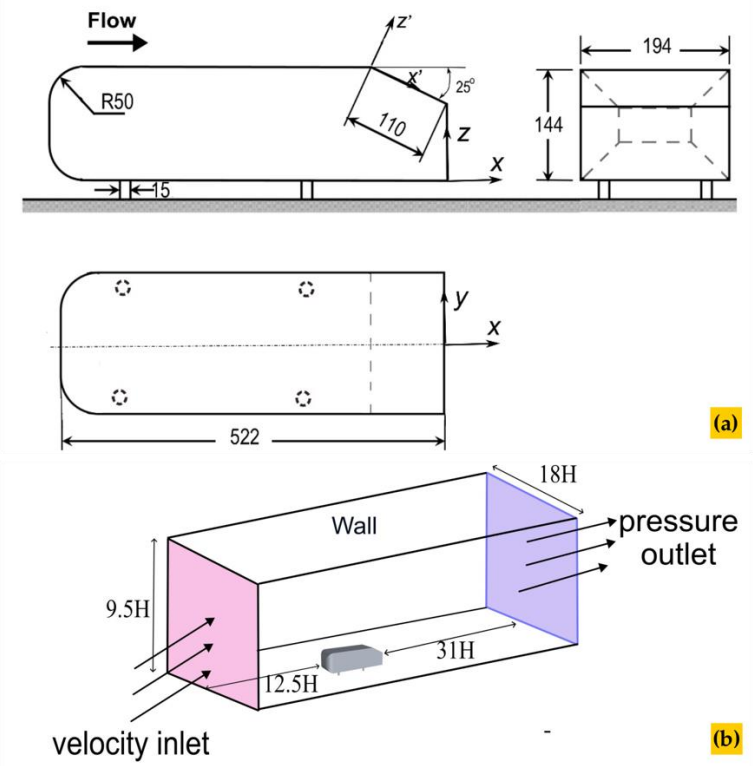

Figure 1. Numerical model and numerical domain (unit in mm): (a) Numerical model; (b) Numerical domain

2.2. *Numerical Conditions*

The numerical simulation is conducted in this study by using Ansys Fluent software. Reynolds averaged Navier-Stokes equations (RANS) with turbulent model *k-ω* SST is used in this study for a discrete scheme. Although the RANS allows only averaged flow fields, it is sufficient for obtaining the drag of the model. The method was widely applied in previous studies. Here, the turbulent model *k-ω* SST is mixed between the *k-ω* model for the flow close to the surface and *k- ε* for the flow far from the model. Consequently, this numerical model is capable of operating as a low-Reynolds turbulence model without the need for extra damping functions. Moreover, the formulation seamlessly shifts to the *k-ε* behavior for the far-field flow, effectively resolving the issue in *k-ω* models where sensitivity to the turbulence characteristics of the incoming flow. Note that since the flow velocity in this study is low, the energy equations were ignored in the numerical process to save numerical time. However, the accuracy of the numerical method was ensured as shown later by the validation process.

The coupled scheme for pressure velocity coupling solver (COUPLED) with a secondary order of accuracy was used in this study for the high accuracy of the results. In this numerical scheme, all variables of continuity, momentum, and turbulence equations are solved simultaneously, which shows a high efficiency, and numerical stability for the results. Since numerical simulation is conducted at low velocity, the air density is considered at zero value. The inlet velocity is set at 20 m/s, providing a based-height Reynolds number of 2×10^5. The freestream velocity, Reynolds number, and models are the same as experimental data by Tran et al. [9].

2.3. *Mesh Independence Study*

The effect of mesh size on the aerodynamic drag of the model is investigated for calculating mesh. Here, the initial thickness of the mesh around the model remains the same for all cases, while the other position is changed. The results of the mesh independence study are shown in **Table 2**. As can be seen the drag increases and becomes stable when the size of the mesh is above 2.0 million cells. The mesh with around 2.4 million cells is selected for all cases to save numerical time and accurate results. Note that the reasonable mesh size for studying flow around Ahmed body by RANS methods is around 2-3 million cells. A similar mesh size was also studied by Viswanathan [23].

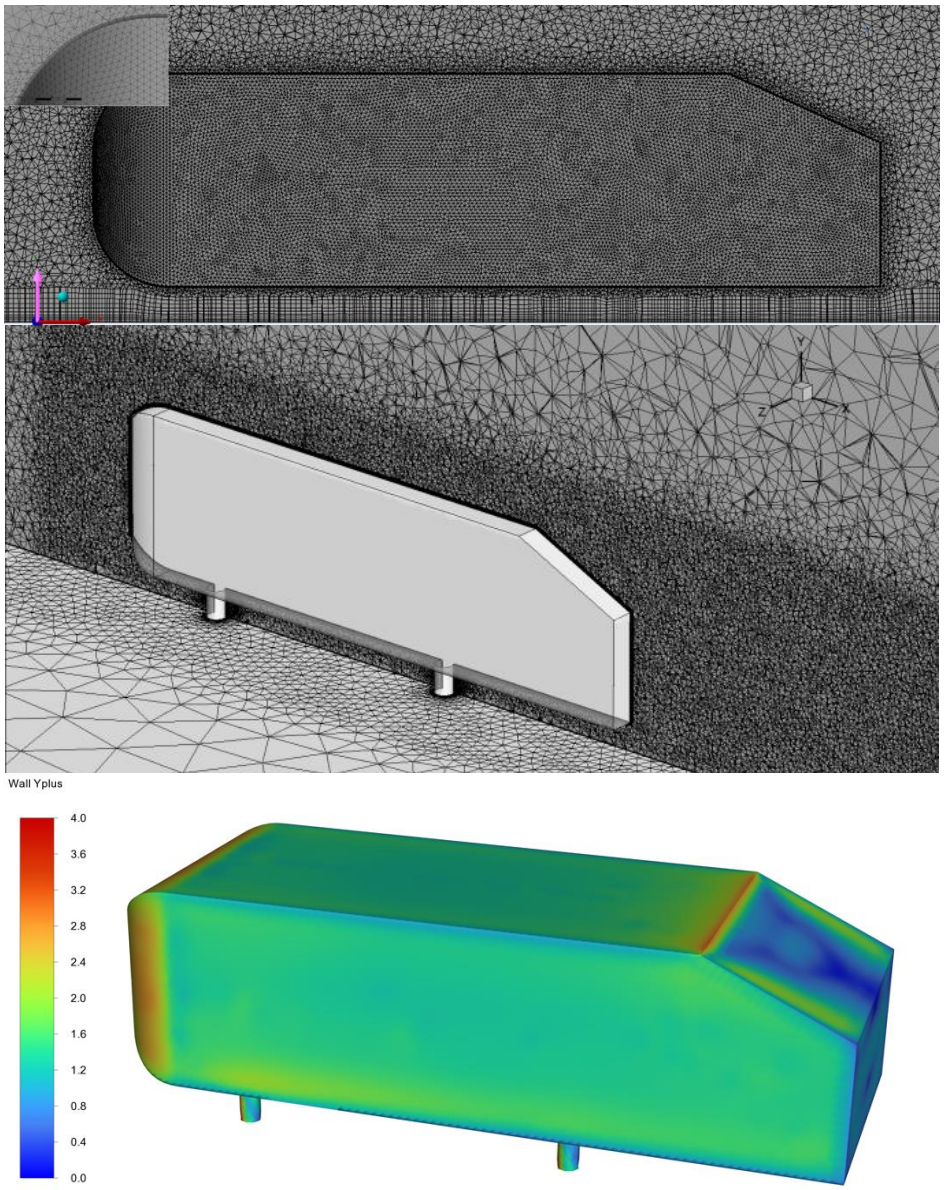

Figure 2. Mesh distribution around the model and y^+ distribution.

Table 2. Effect of mesh size on aerodynamic drag and maximum y^+ of the model

Cell number (× 10^6)	y^+	C_D
0.380	2.5	0.4029
0.642	2	0.3901
0.815	2	0.3900
1.041	1.5	0.3651
1.470	1.3	0.3648
2.108	1.3	0.3651

2.4. *Adjustment of the Numerical Parameter*

It should be noted that previous studies failed to capture flow structure on slant surfaces by the RANS model [16], [17]. Guilmineau et al. [16], who examined the different simulation models, for example, indicated that the RANS methods cannot show good results for surface flow on the slant of the Ahmed body. The reason for that problem is the overestimation of eddy viscosity in the high reversed flow region. Consequently, the fully separated flow is often observed for the 25° Ahmed body in simulation studies [17]. Generally, high accurate numerical scheme, such as a large eddy simulation, should be used to capture correct the flow structure on the slant. In this study, the turbulent model k-ω SST is applied for the simulation. In this model, additional equations are used for determining the turbulent kinetic energy k and the specific dissipation rate ω. The system equations for k and ω can be written as Eq. (1).

As the two parameters k and ω are found (Eq. (1)), the eddy-viscosity ν_t calculated as Eq. (2).

$$\frac{\partial(\rho k)}{\partial t}+\frac{\partial(\rho u_j k)}{\partial x_j}=P-\beta^*\rho\omega k+\frac{\partial}{\partial x_j}\left[(\mu+\sigma_k\mu_t)\frac{\partial k}{\partial x_j}\right]$$
$$\frac{\partial(\rho\omega)}{\partial t}+\frac{\partial(\rho u_j\omega)}{\partial x_j}=\frac{\gamma}{v_t}P-\beta\rho\omega^2+\frac{\partial}{\partial x_j}\left[(\mu+\sigma_k\mu_t)\frac{\partial\omega}{\partial x_j}\right]+2(1-F_1)\frac{\rho\sigma_{\omega2}}{\omega}\frac{\partial k}{\partial x_j}\frac{\partial\omega}{\partial x_j} \quad (1)$$

$$v_t=\frac{a_1 k}{\max(a_1\omega;\Omega F_2}} \quad (2)$$

Where,

$$F_2=tanh\left[\left[max\left(\frac{2\sqrt{k}}{\beta\omega y},\frac{500v}{y^2\omega}\right)\right]^2\right] \quad (3)$$

$$P_k=\min\left(\tau_{ij}\frac{\partial U_i}{\partial x_j},10\beta k\omega\right) \quad (4)$$

$$F_1=tanh\left\{\left\{min\left[max\left(\frac{\sqrt{k}}{\beta\omega y},\frac{500v}{y^2\omega}\right),\frac{4\sigma_{\omega2}k}{CD_{k\omega}y^2}\right]\right\}^4\right\} \quad (5)$$

$$CD_{k\omega}=\max\left(2\rho\sigma_{\omega2}\frac{1}{\omega}\frac{\partial k}{\partial x_i}\frac{\partial\omega}{\partial x_i},10^{-10}\right) \quad (6)$$

$$\phi=\phi_1F_1+\phi_2(1-F_1) \quad (7)$$

In the above equations, σ_k, $\sigma_{\omega2}$, β, β^*, κ, and γ are model constant parameters. The criteria for selecting those numbers were presented in previous studies by Menter [24]. Those parameters are determined as follows:

α_1	$=\frac{5}{9}$	β_1	$=\frac{3}{40}$
α_2	= 0.44	β_2	= 0.0828
σ_{k1}	= 0.85	β^*	= 0.09
σ_{k2}	= 1	$\sigma_{\omega1}$	= 0.5
		$\sigma_{\omega2}$	= 0.856

Literature showed that the viscosity ν_t can be changed widely in separation flow [25], [26]. Consequently, the accurate prediction of eddy viscosity is essential to capture the flow separation under a strong pressure gradient. From Eq. (2) we see that the coefficient a_1 may change the value of the viscosity ν_t. Jonson-King [25] proposed a relation $\nu_t = \rho a_1 k$ for the shear-stress formulation to avoid the excessive value in adverse pressure gradient regions. The modification of parameter a_1 was found to better predict the nozzle flow by Chiebi et al. [27], and flow over airfoil by Matyushenko and Garbaruk [26] Notably, a similar approach by Jonson-King [25] was used by Menter [24] to estimate the turbulent viscosity in SST k-ω model, which was resulted in the failed prediction of the flow separation on the Ahmed body, previously. In our initial calculation with standard parameters, the turbulent model k-ω SST model overestimates flow behavior around the Ahmed body. Consequently, it is suggested that increasing coefficient a_1 in simulation is a way to improve the numerical results [27].

In this study, the coefficient a_1 is changed from 0.31 to 2.00 for exanimating the results. The effect of coefficient a_1 on flow on the slant and drag of the model at zero yaw angle is shown in **Figure 3** and **Figure 4**. Here, the x-axis was normalized by the width W of the model. The position $y/W = 0$ is at the centerline of the model as shown in **Figure 1**. The y-axis presents the position of the model on the slant surface. S means the total length of the slant. The coefficient a_1 has a strong effect on the flow at the upper surface while the drag coefficient changes little. At a high coefficient, the length of the separation bubble on the surface is short, which is different from experimental data. The initial test is also conducted for different yaw angles between 0 and 15°. The $a_1 = 0.36$ is selected for calculation because the results are reasonable and comparable to experimental data. Note that at $a_1 = 0.36$, the difference of drag between the current and previous experimental data by Tran et al. [9] is at around 0.73%.

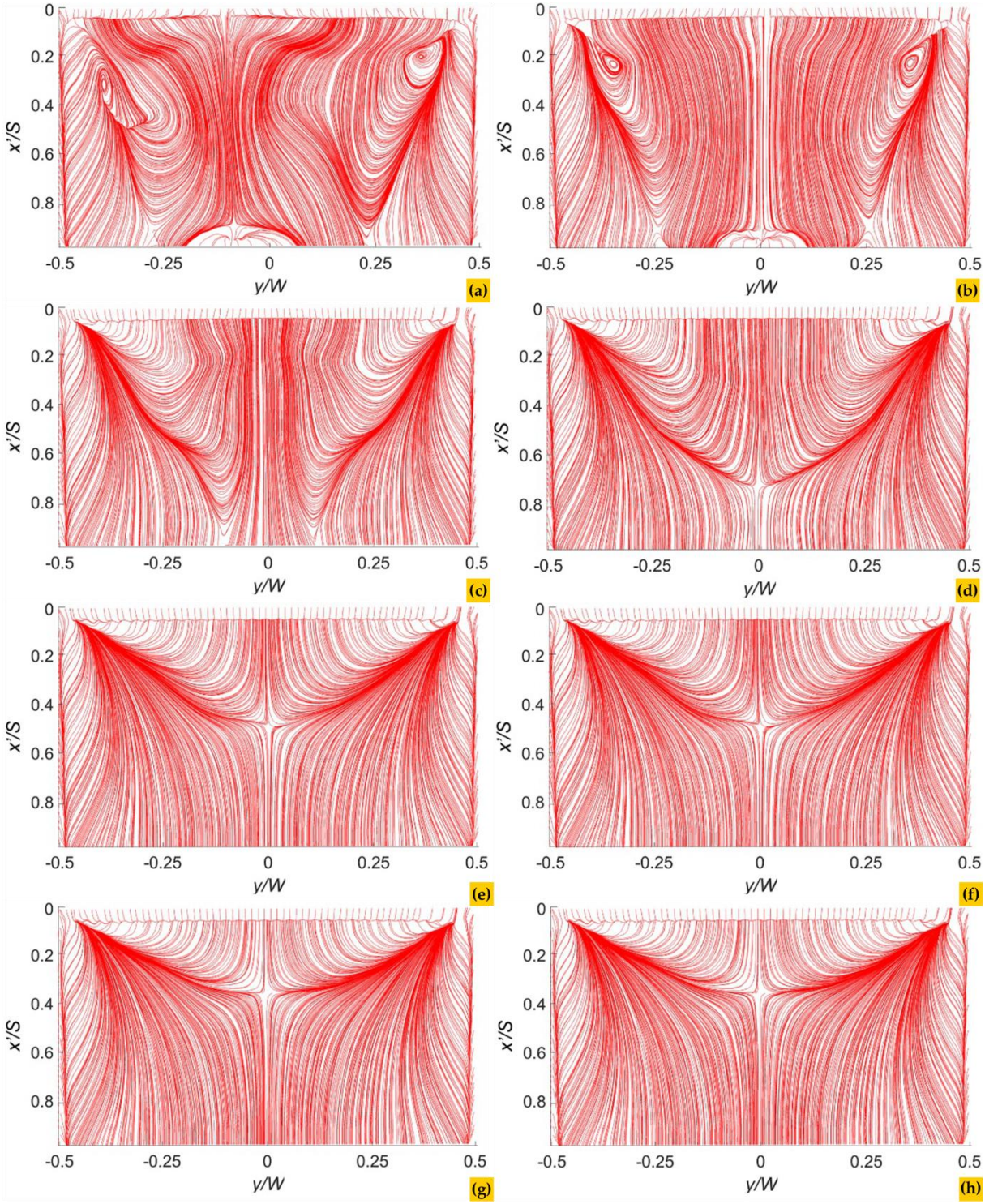

Figure 3. Effect of coefficient a_1 on skin-friction fields on the slant: (a) 0.31; (b) 0.33; (c) 0.35; (d) 0.36; (e) 0.40; (f) 0.50; (g) 1.00; (h) 2.00

3. Results and Discussion

3.1. *Aerodynamic Force of the Model*

Figure 5 shows the aerodynamic drag of the model for different yaw angles. The experimental results by Tran et al. [9] at the same flow conditions were also added for comparison. The numerical results are close to experimental data at low yaw angles. The aerodynamic drag quickly increases with yaw angles and different results were observed for numerical and experimental methods. This is probably due to the slight difference in the flow and experimental setup between experiments and numerical studies. However, the trend of drag with increasing yaw

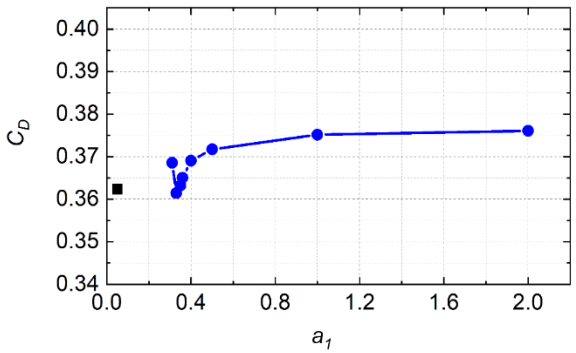

Figure 4. Effect of coefficient a1 on aerodynamic drag of the model (the square black point shows the experimental results by Tran et al. [7])

angles is similar in both methods. At yaw angles of around 15°, the aerodynamic drag increases double and it reaches three times at yaw angles of around 25°. The results are similar to the previous observation by Millan et al. [11], who measured the drag of the Ahmed body for yaw angles from 0 to 90°. The increasing yaw angles also lead to the growth of upside force and lift of the models. However, only the drag coefficient was measured in the previous study [11] due to the limitation of the facility. The advantage of computational simulation allows to extract all three components of the force and provides more detailed information.

Interestingly, the lift of the model increases to yaw angles of around 30° then it drops for higher yaw angles. Detailed analysis for skin-friction fields shown later in **Figure 7** and **Figure 8** indicates that the separation bubble disappears at an angle above 30°. Additionally, the pressure distribution on the slant will be analyzed to understand the reason for decreasing lift. We will show that the main reason for reducing lift is connected to the development of the longitudinal vortex on the windward side (**Figure 8**), which changes the pressure distribution on the slant as shown in **Figure 9**, and pressure drag acting on the slant (**Figure 6**). Here, the trend of the lift coefficient was not presented in the previous study [11].

Previously, Tran et al. [9] showed that the increasing drag of the model is mainly associated with increasing pressure drag acting on the slant and base surfaces. In this study, we present the pressure drag acting on the slant to understand its effect on the total drag. The results of pressure drag acting on the slant, which were integrated from the pressure distribution on the surface, for different yaw angles are drawn in **Figure 6**. It is interestingly that the drag increases with yaw angles up to. However, the values decrease for higher yaw angles. The flow phenomenon on the slant will be analyzed in more detail. Note that the

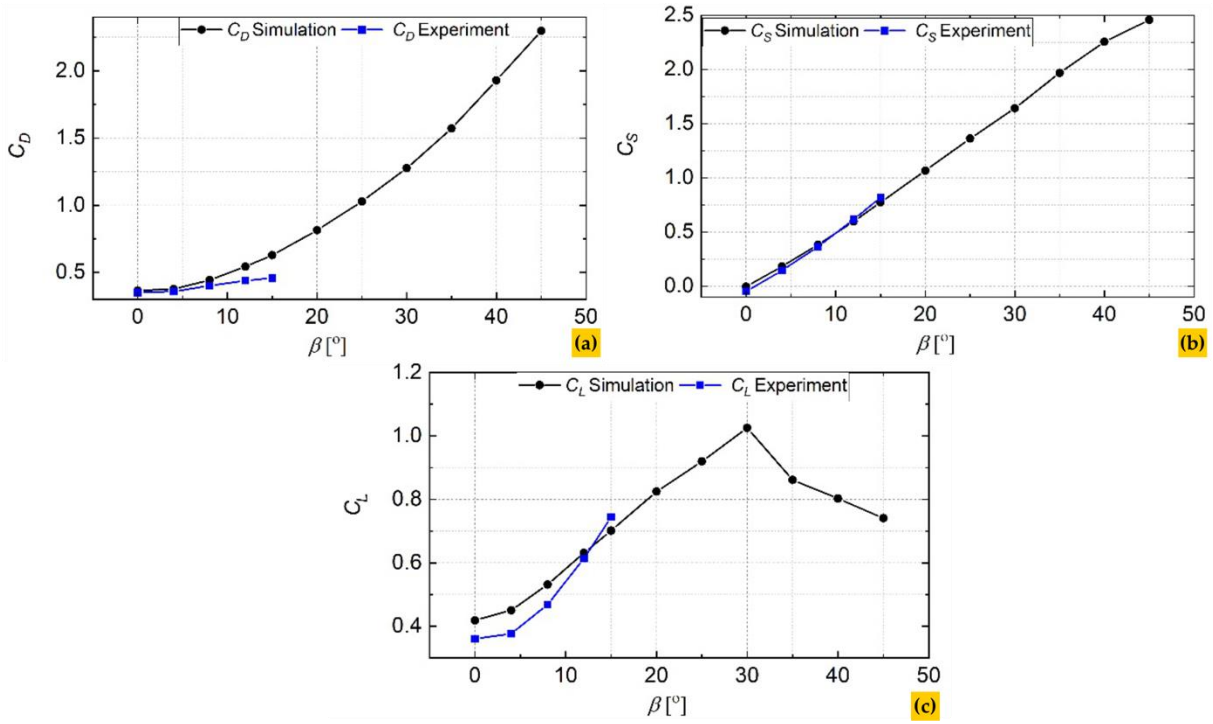

Figure 5. Aerodynamic forces of the model as a function of yaw angles: (a) Drag coefficient; (b) Side coefficient; (c) Lift coefficient

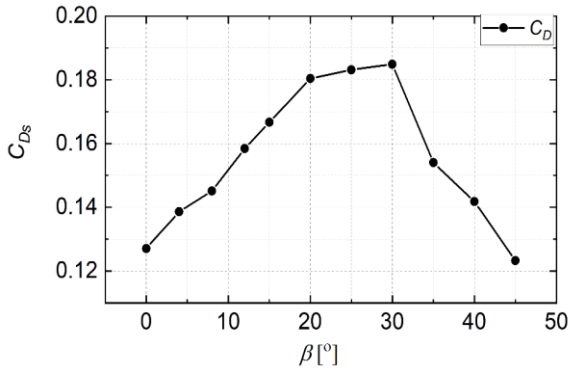

Figure 6. Pressure drag acting on the slant surface

measurement drag component is sufficiently complicated for experimental studies. Tran et al. [28], for example, used pressure taps to integrate pressure drag components. However, due to the limitation of pressure tap numbers, the results may have some level of uncertainty. The pressure drag acting on the slant extracted in this study allows to understand the detailed reason for the lift trend at high yaw angles.

3.2. *Skin-friction Fields on the Slant*

Figure 7 shows the skin friction fields on the slant for different yaw angles. At the yaw angle of 0°, the flow shows highly symmetric concerning the line y= 0 with a large separation bubble on the surface. The structure and length of the separation bubble are similar to experimental results obtained by Tran et al. [7] and other previous studies. The numerical results also confirm that the flow is separated behind the leading edge of the slant. Generally, the RANS with *k-ω* SST turbulent model provides over-estimated results for the flow on the slant as shown by other previous studies. However, with some adjustments shown in section 2.3, the current method can provide sufficiently good results of the surface flow. The flow structure on the slant for a yaw angle of 4° is similar to the case of 0°, except for the decrease's region with reversed flow on the windward side. The length of the separation bubble at the centerline and flow structure on the leeward side is comparable to the baseline case. For yaw angles above 4°, the flow structure on the slant is highly modified. In detail, the separation bubble moves to the leeward side and its structure becomes smaller in both length and width. At yaw angles above 30°, the separation bubble almost disappears on the slant. The longitudinal vortex on the windward develops and becomes remarkably with increasing yaw angles. The pattern of this skin-friction results is shown firstly in the current study. It is suggested to select those numerical parameters for the surface flow on the slant of the Ahmed body.

3.3. *Flow Structure around the Slant*

To understand the structure of the longitudinal vortexes on the slant, the skin-friction streamlines around the back of the model are shown in **Figure 8.** Clearly, the change of flow with the yaw angle occurs from the roof surfaces. A longitudinal vortex is generated on the root surface at the windward side for the yaw angle of 8°. This structure develops and can be seen clearly at yaw angles above 15°. The longitudinal vortex strongly affects flow on the slant and base surfaces. At yaw angles of 35°, the longitudinal vortex develops on the total leading edge of the slant. Inside the longitudinal vortex on the windward side, a large secondary separation and reattachment flow can be observed. This structure flow is significantly large, which results in changing flow on the slant surface. However, the flow on the vertical bases is slightly changed for yaw angles from 8° to 35°. At the yaw angle of 45°, the structure of base flow changes from horizontal to vertical directions.

3.4. *Mean Pressure Coefficient on the Slant*

Figure 9 shows the mean pressure coefficient on the slant for different yaw angles. The low-pressure region on the surface is connected to the generation of the longitudinal vortexes and the separation bubble on the slant. The low-pressure region extends on the windward side and moves inboard with increasing yaw angles. Generally, the pressure is significantly low around the leading edges of the slant. At the yaw angle of around 35°, the region with low pressure on the slant reaches maximum. Interestingly, at the yaw angle of 40°, the pressure becomes a flat distribution and the low-pressure region disappears. It is expected that the longitudinal vortex on the windward side moves upward, which has little effect on the flow at the upper surface. The change of the pressure coefficient on the slant for different yaw angles is similar to previous observation by Tran et al. [6], [9]. However, previous studies were conducted for only yaw angles up to 15°. By applying numerical

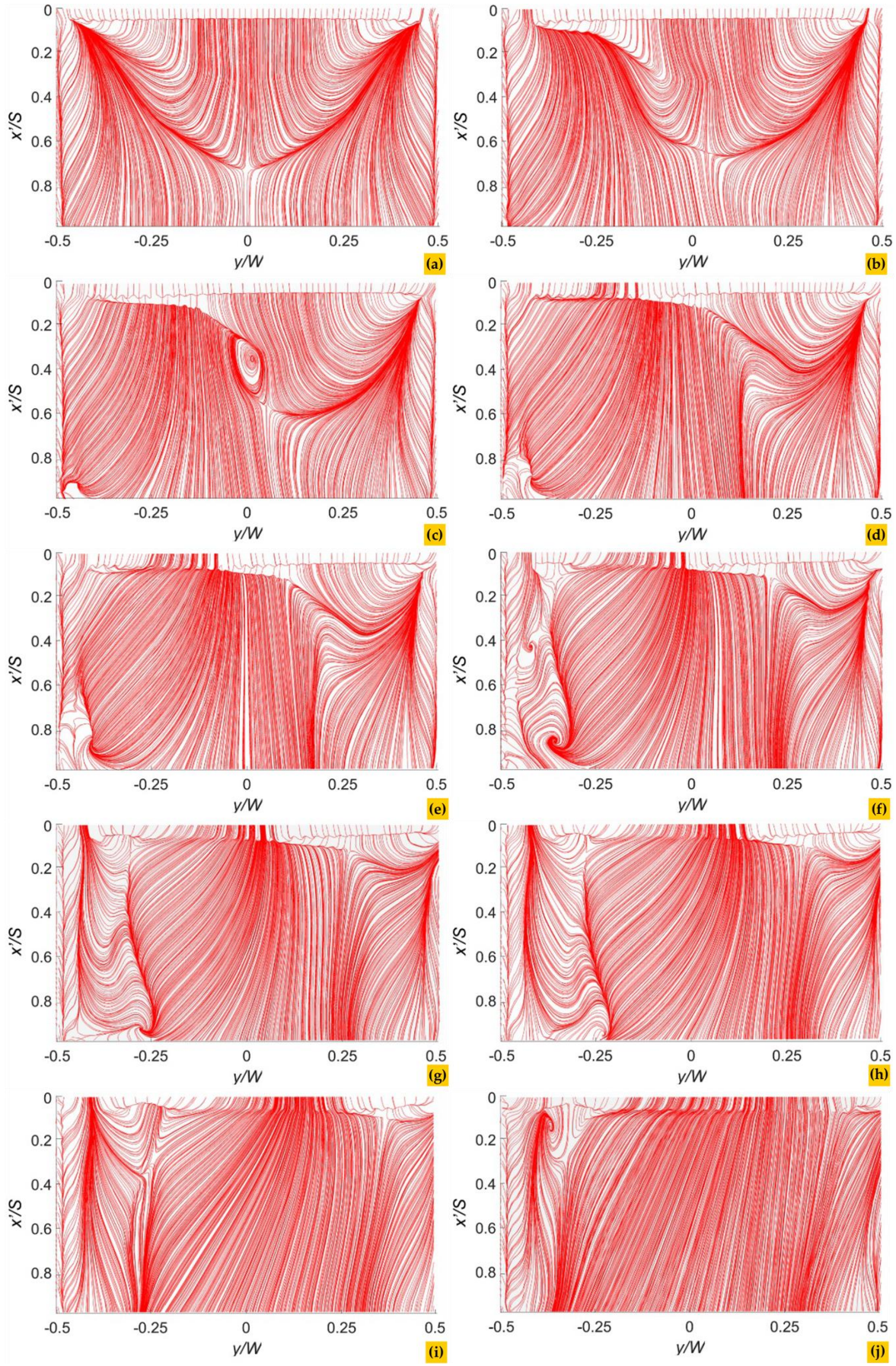

Figure 7. Skin-friction streamlines on the slant surface with β: (a) 0°; (b) 4°; (c) 8°; (d) 12°; (e) 15°; (f) 20°; (g) 25°; (h) 30°; (i) 35°; (j) 40°

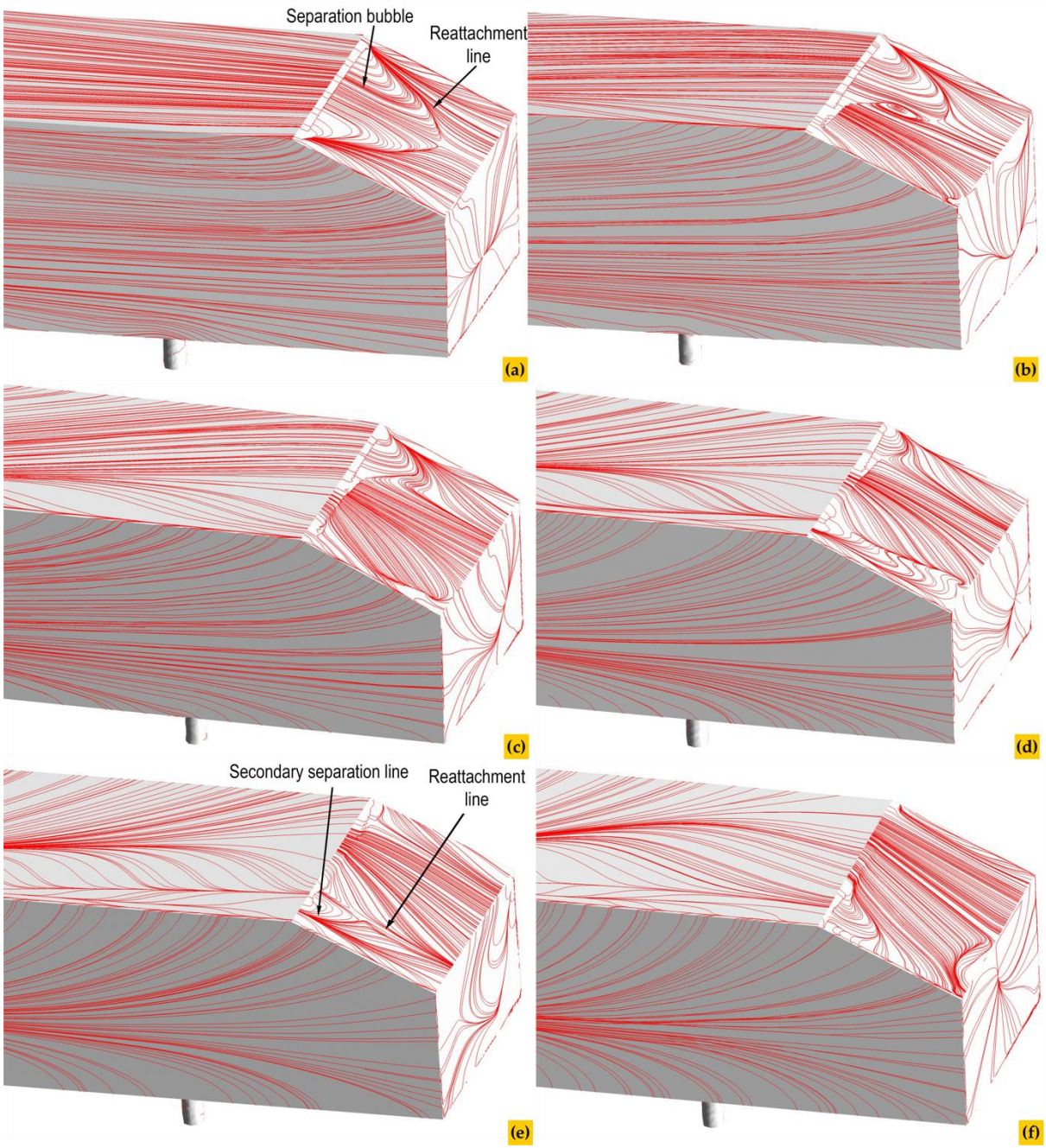

Figure 8. Skin friction streamlines around the rear surface with β: (a) 0°; (b) 8°; (c) 15°; (d) 25°; (e) 35°; (f) 45°

simulation, this study extracts the flow feature on the slant for higher yaw angles, which is up to 40°. The difference trend with previous observation occurs for the yaw angle of 40° and it stands for the novel result of the current study. Note that studying the flow around slant at sufficient high yaw angles is important because critical weather conditions may occur in real engineering applications and have a strong effect on the performance of the vehicles.

3.5. Wake Flow at Different Yaw Angles

Figure 10 shows the averaged wake structure on the symmetric plane of the model. At zero yaw angle, the wake structure is featured by two vortexes at the base, which is similar to other previous studies by Tran et al. [6], [9]. With increasing yaw angles up to 25°, the length of the near wake becomes shorter. The wake structure changes for yaw angles above 30°. At the yaw angle of 40°, the separation flow occurs above the

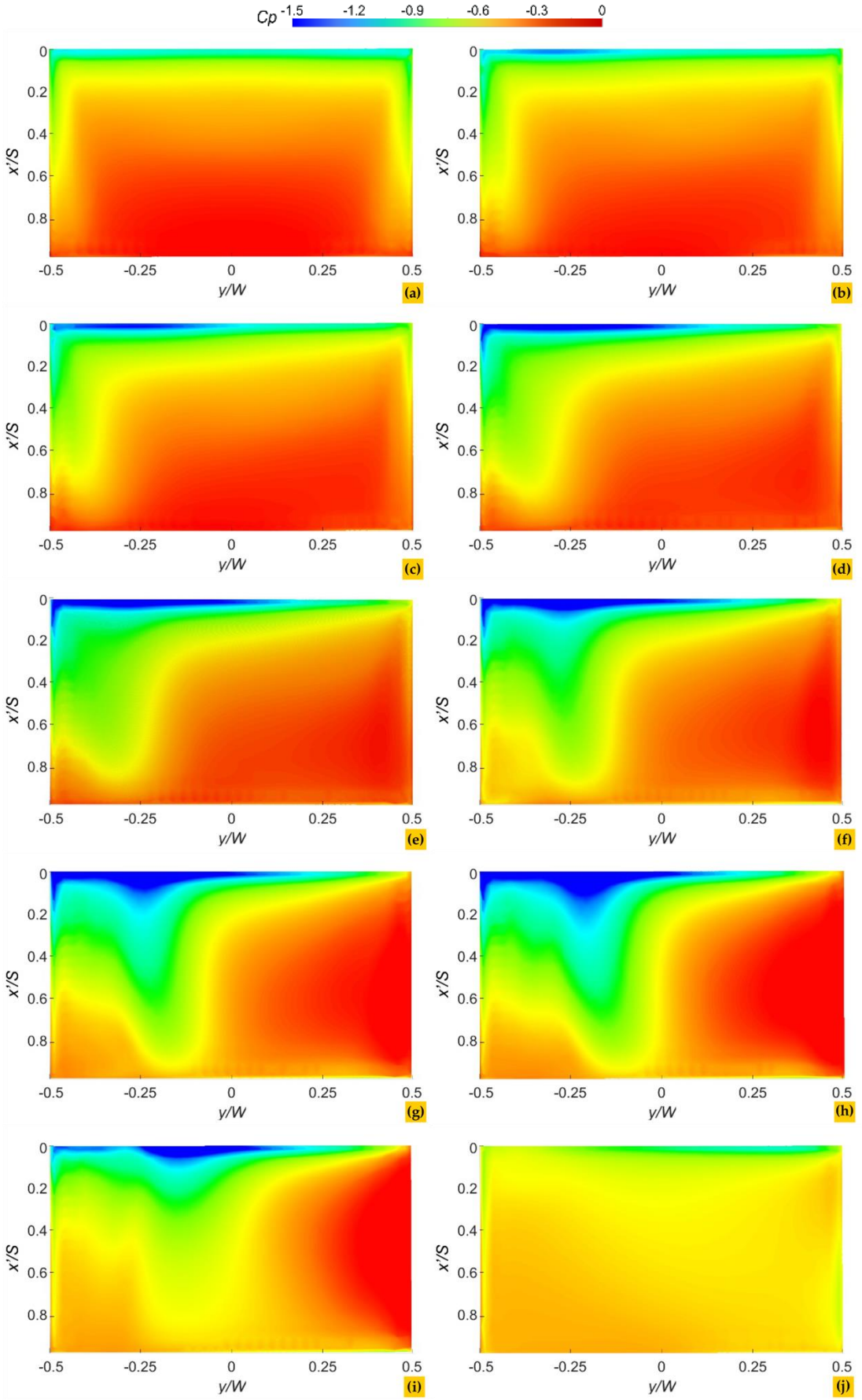

Figure 9. Mean pressure coefficient on the slant for different yaw angle with β: (a) 0°; (b) 4°; (c) 8°; (d) 12°; (e) 15°; (f) 20°; (g) 25°; (h) 30°; (i) 35°; (j) 40°

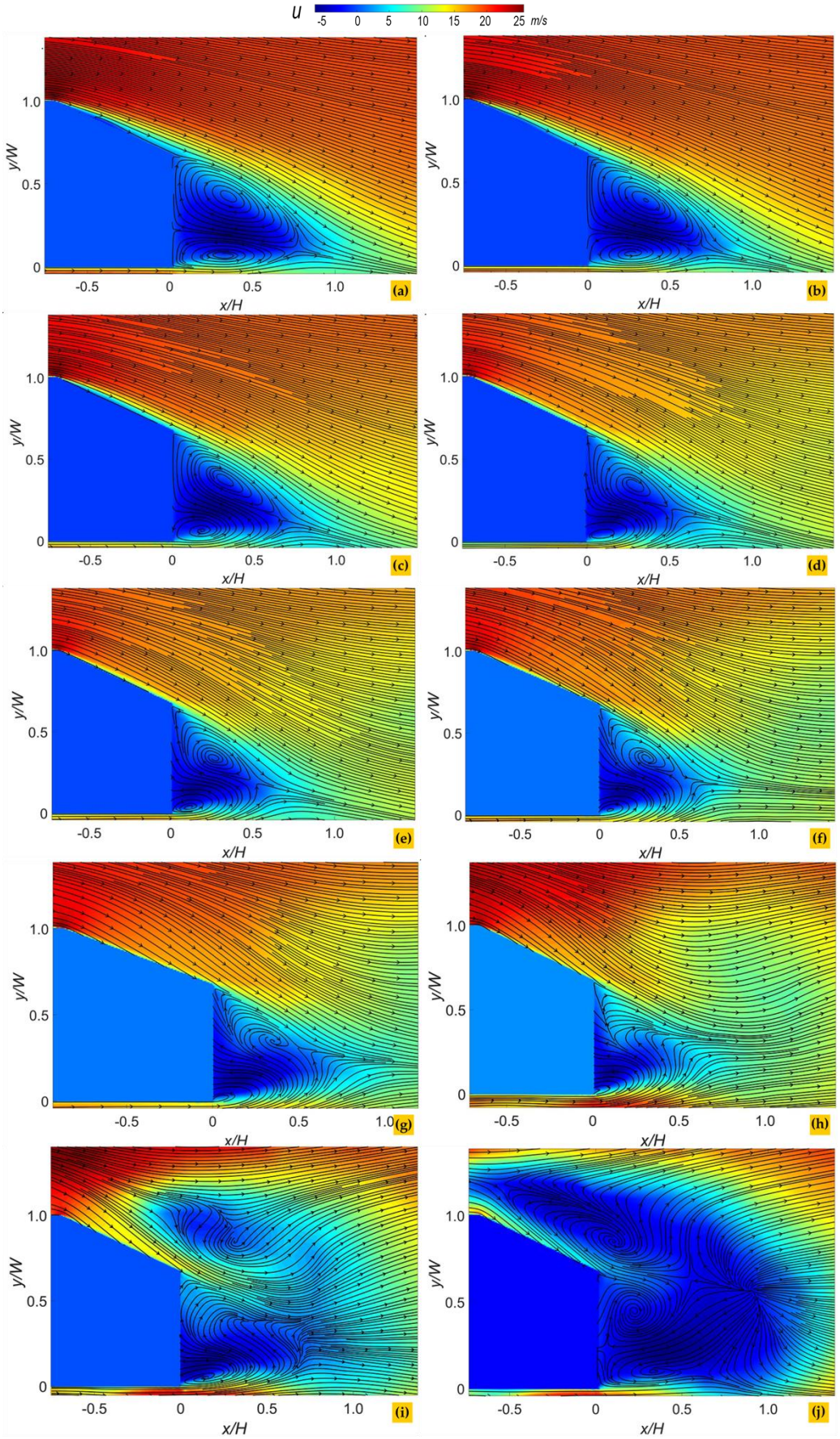

Figure 10. Wake at the centerline of the model with yaw angles with β: (a) 0°; (b) 4°; (c) 8°; (d) 12°; (e) 15°; (f) 20°; (g) 25°; (h) 30°; (i) 35°; (j) 40°

slant, resulting in a large wake structure. The large wake structure is a reason for the increasing drag of the model. The wake structure at high yaw angles is an interesting phenomenon, which should be further investigated for more detailed understanding, particularly for unsteady flow behavior.

Figure 11 shows the flow on the cross-sectional plane at x/L = 1.2 of the model for different yaw angles mapping with vorticity values. Here, ω is the two-component vorticity in the cross-section plane, which is calculated by Eq. (8) and ω^* is the maximum value of the vorticity for the model at the yaw angle of zero degree. At zero yaw angle, the flow structure shows high symmetry with respect to the line z/H = 0. Two vortice pairs are observed around the model at the upper and lower surfaces. The strength of the vortexes pair at the upper surface is remarkably high and corresponds to the existence of two longitudinal vortexes on the slant surface. This feature was highly consistent with previous observations by Tunay et al. [7], [19] in zero yaw angle. The vortex center on the windward side moves upward with yaw angles. The upward movement of the longitudinal vortex on the windward side is the reason for increased pressure on the slant as a result. The strength of lower vortexes is small and results from the interaction between the model and the ground surface. As the yaw angle increases, the longitudinal vortex on the windward side develops and moves upward while the vortex on the leeward side becomes small and disappears. On the opposite side, the ground vortex on the windward side moves to the model while the vortex on the leeward side develops with yaw angles. At a yaw angle of around 40°, this structure disappears. Note that the vortex structure on the cross-sectional plane was not taken attention in previous studies for the Ahmed body during the yaw conditions. This feature was extracted well in the current study by the numerical process.

$$\omega = \frac{\partial v}{\partial z} - \frac{\partial w}{\partial y} \tag{8}$$

4. Conclusion

Flow around the Ahmed body during crosswind conditions was presented in this study. The yaw angles were changed from 0 to 45° to understand their effect on the flow structure around the slant and aerodynamic forces of the model. Numerical simulation based on the RANS k-ω SST model with some adjustments was applied in this study for analyzing the complex flow. The results indicate that the current method shows a good ability to predict flow behavior around the model. The numerical results showed close results to experimental data for yaw angles between 0 and 8°. At high yaw angles, longitudinal vortexes develop strongly and move upward on the windward side, which results in the disappearance of the separation flow on the slant surface. The leeward side becomes small and disappears with increasing yaw angles. The lift of the model and pressure drag acting on the slant decrease at a yaw angle above 35°, which results from the movement of longitudinal vortexes at the upper surface. The results also lead to a change in pressure distribution on the surface. The surface flow indicates that the size of the separation bubble decreases and it disappears at high yaw angles.

This study was conducted for the Reynolds number of around 2×10^5, but the results can be applied to higher Reynolds numbers. Additionally, it is believed that the main features should occur for the real vehicles with similar slant angles. However, further studies are required to confirm the results. Additionally, it is suggested that studying the wake flow at high yaw angles up to 40° is important because critical weather conditions may occur in real engineering applications and have a strong effect on the performance of the vehicles

Although the averaged surface flow of the slant was captured well by the current RANS simulation method, a higher numerical scheme should be conducted for the Ahmed body during yaw conditions to understand the unsteady behavior. Additionally, studies for real vehicles in real conditions should be conducted to classify the difference between the research and real vehicles.

Acknowledgments

Pham Van Duy was supported by VinIF for a master degree under grant number VINIF.2023.ThS.026.

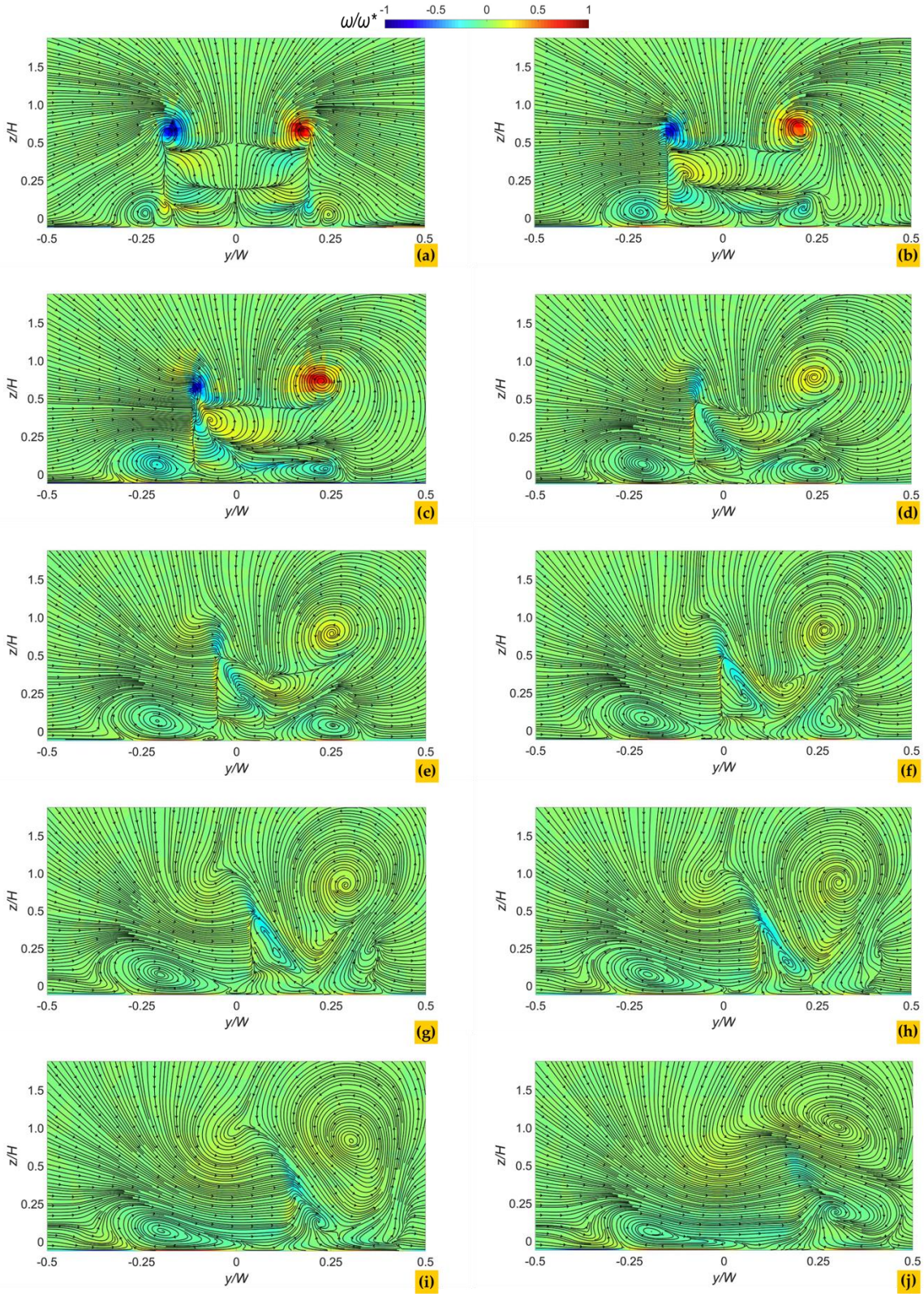

Figure 11. Wake at the cross-sectional plane of the model with yaw angles with β: (a) 0°; (b) 4°; (c) 8°; (d) 12°; (e) 15°; (f) 20°; (g) 25°; (h) 30°; (i) 35°; (j) 40°

Author's Declaration

Authors' contributions and responsibilities

Pham Van Duy: Methodology, Investigation, Analyzing, Writing – review & editing Writing. Le Dinh Anh: Conceptualization, Methodology, Investigation, Writing – review & editing. Dinh Cong Truong: Conceptualization, Methodology, Investigation. Tran The Hung: Conceptualization, Methodology, Investigation, Writing – review & editing Writing, Analyzing, Reviewing and Editing.

Do Van Minh: Writing – review & editing Writing, Analyzing, Reviewing and Editing

Funding

This research is funded by the Vingroup Innovation Foundation (VinIF) under the domestic master's training program in 2023 (Scholarship Code VINIF.2023.ThS.026).

Availability of data and materials

All data are available from the authors.

Competing interests

The authors declare no competing interest.

Additional information

No additional information from the authors.

References

[1] D. Kim, H. Lee, W. Yi, and H. Choi, "A bio-inspired device for drag reduction on a three-dimensional model vehicle," *Bioinspiration and Biomimetics*, vol. 11, no. 2, 2016, doi: 10.1088/1748-3190/11/2/026004.

[2] S. R. Ahmed, G. Ramm, and G. Faltin, "Some Salient Features of the Time -Averaged Ground," *SAE Transactions*, vol. 93, no. 1984, pp. 473–503, 1984.

[3] A. K. Perry, G. Pavia, and M. Passmore, "Influence of short rear end tapers on the wake of a simplified square-back vehicle: wake topology and rear drag," *Experiments in Fluids*, vol. 57, no. 11, pp. 1–17, 2016, doi: 10.1007/s00348-016-2260-3.

[4] Y. A. Irving Brown, S. Windsor, and A. P. Gaylard, "The effect of base bleed and rear cavities on the drag of an SUV," *SAE Technical Papers*, 2010, doi: 10.4271/2010-01-0512.

[5] Z. Arifin *et al.*, "Aerodynamic Characteristics of Ahmed Body with Inverted Airfoil Eppler 423 and Gurney Flap on Fastback Car," *Automotive Experiences*, vol. 5, no. 3, pp. 355–370, 2022, doi: 10.31603/ae.7067.

[6] T. The Hung, M. Hijikuro, M. Anyoji, T. Uchida, T. Nakashima, and K. Shimizu, "Deflector effect on flow behavior and drag of an Ahmed body under crosswind conditions," *Journal of Wind Engineering and Industrial Aerodynamics*, vol. 231, p. 105238, Dec. 2022, doi: 10.1016/j.jweia.2022.105238.

[7] T. Tunay, B. Yaniktepe, and B. Sahin, "Computational and experimental investigations of the vortical flow structures in the near wake region downstream of the Ahmed vehicle model," *Journal of Wind Engineering and Industrial Aerodynamics*, vol. 159, no. October, pp. 48–64, 2016, doi: 10.1016/j.jweia.2016.10.006.

[8] A. D. Le, H. Phan Thanh, and H. Tran The, "Assessment of a Homogeneous Model for Simulating a Cavitating Flow in Water Under a Wide Range of Temperatures," *Journal of Fluids Engineering*, vol. 143, no. 10, p. 101204, 2021, doi: 10.1115/1.4051078.

[9] T. H. Tran, M. Anyoji, T. Nakashima, K. Shimizu, and A. D. Le, "Experimental Study of the Skin-Friction Topology Around the Ahmed Body in Cross-Wind Conditions," *Journal of Fluids Engineering*, vol. 144, no. 3, 2022, doi: 10.1115/1.4052418.

[10] G. Bonnavion *et al.*, "On multistabilities of real car's wake," *Journal of Wind Engineering and Industrial Aerodynamics*, vol. 164, no. January, pp. 22–33, 2017, doi: 10.1016/j.jweia.2017.02.004.

[11] F. J. Bello-Millán, T. Mäkelä, L. Parras, C. del Pino, and C. Ferrera, "Experimental study on Ahmed's body drag coefficient for different yaw angles," *Journal of Wind Engineering and Industrial Aerodynamics*, vol. 157, pp. 140–144, Oct. 2016, doi: 10.1016/j.jweia.2016.08.005.

[12] A. Sciacchitano and D. Giaquinta, "Investigation of the Ahmed body cross-wind flow topology by robotic volumetric PIV," 2019.

[13] T. Tunay, B. Sahin, and H. Akilli, "Experimental and numerical studies of the flow around the Ahmed body," *Wind and Structures*, vol. 17, no. 5, pp. 515–535, 2013, doi: 10.12989/was.2013.17.5.515.

[14] W. Meile, T. Ladinek, G. Brenn, A. Reppenhagen, and A. Fuchs, "Non-symmetric bi-stable flow around the Ahmed body," *International journal of heat and fluid flow*, vol. 57, pp. 34–47, 2016, doi: 10.1016/j.ijheatfluidflow.2015.11.002.

[15] T. H. Tran, H. Q. Dinh, H. Q. Chu, V. Q. Duong, C. Pham, and V. M. Do, "Effect of boattail angle on near-wake flow and drag of axisymmetric models: a numerical approach," *Journal of Mechanical Science and Technology*, vol. 35, no. 2, pp. 563–573, Feb. 2021, doi: 10.1007/s12206-021-0115-1.

[16] E. Guilmineau, G. B. Deng, A. Leroyer, P. Queutey, M. Visonneau, and J. Wackers, "Assessment of hybrid RANS-LES formulations for flow simulation around the Ahmed body," *Computers and Fluids*, vol. 176, no. January, pp. 302–319, 2018, doi: 10.1016/j.compfluid.2017.01.005.

[17] F. Delassaux, I. Mortazavi, E. Itam, V. Herbert, and C. Ribes, "Sensitivity analysis of hybrid methods for the flow around the ahmed body with application to passive control with rounded edges," *Computers and Fluids*, vol. 214, p. 104757, 2021, doi: 10.1016/j.compfluid.2020.104757.

[18] C. H. Tsai, L. M. Fu, C. H. Tai, Y. L. Huang, and J. C. Leong, "Computational aero-acoustic analysis of a passenger car with a rear spoiler," *Applied Mathematical Modelling*, vol. 33, no. 9, pp. 3661–3673, 2009, doi: 10.1016/j.apm.2008.12.004.

[19] T. Tunay, E. Firat, and B. Sahin, "Experimental investigation of the flow around a simplified ground vehicle under effects of the steady crosswind," *International Journal of Heat and Fluid Flow*, 2018, doi: 10.1016/j.ijheatfluidflow.2018.03.020.

[20] A. Rao, G. Minelli, B. Basara, and S. Krajnović, "On the two flow states in the wake of a hatchback Ahmed body," *Journal of Wind Engineering and Industrial Aerodynamics*, vol. 173, no. June 2017, pp. 262–278, 2018, doi: 10.1016/j.jweia.2017.10.021.

[21] T. Nakashima, T. Moriuchi, Y. Chao, and I. Kohri, "Wake flow visualization of a simplified vehicle model during flow state change," *ASME-JSME-KSME 2019 8th Joint Fluids Engineering Conference, AJKFluids 2019*, vol. 3A-2019, no. July, 2019, doi: 10.1115/AJKFluids2019-5404.

[22] C. S. Yuan, S. Mansor, and M. A. Abdullah, "Effect of spoiler angle on the aerodynamic performance of hatchback model," *International Journal of Applied Engineering Research*, vol. 12, no. 22, pp. 12927–12933, 2017.

[23] H. Viswanathan, "Aerodynamic performance of several passive vortex generator configurations on an Ahmed body subjected to yaw angles," *Journal of the Brazilian Society of Mechanical Sciences and Engineering*, vol. 43, no. 3, pp. 1–23, 2021, doi: 10.1007/s40430-021-02850-8.

[24] F. R. Menter, "Two-equation eddy-viscosity turbulence models for engineering applications," *AIAA journal*, vol. 32, no. 8, pp. 1598–1605, 1994, doi: 10.2514/3.12149.

[25] D. A. Johnson and L. S. King, "A mathematically simple turbulence closure model for attached and separated turbulent boundary layers," *AIAA Journal*, vol. 23, no. 11, pp. 1684–1692, Nov. 1985, doi: 10.2514/3.9152.

[26] A. A. Matyushenko and A. V. Garbaruk, "Adjustment of the k-ω SST turbulence model for prediction of airfoil characteristics near stall," *Journal of Physics: Conference Series*, vol. 769, no. 1, 2016, doi: 10.1088/1742-6596/769/1/012082.

[27] R. Chebli, B. Audebert, G. Zhang, and O. Coutier-Delgosha, "Influence of the turbulence modeling on the simulation of unsteady cavitating flows," *Computers & Fluids*, vol. 221, p. 104898, 2021, doi: 10.1016/j.compfluid.2021.104898.

[28] T. H. Tran, M. Hijikuro, M. Anyoji, T. Uchida, T. Nakashima, and K. Shimizu, "Surface flow and aerodynamic drag of Ahmed body with deflectors," *Experimental Thermal and Fluid Science*, p. 110887, 2023, doi: 10.1016/j.expthermflusci.2023.110887.